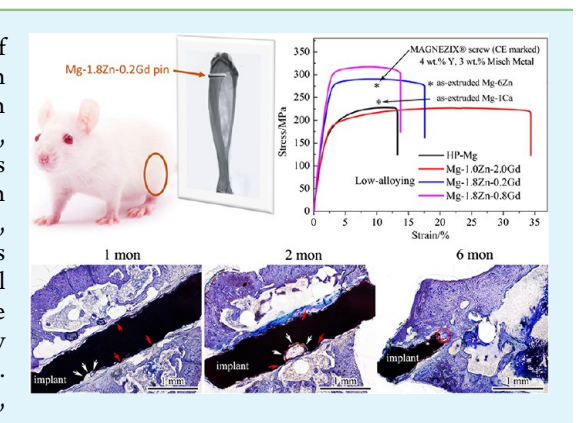
Cite This: ACS Appl. Mater. Interfaces 2018, 10, 4394–4408

# In Vitro and in Vivo Studies on Biomedical Magnesium Low-Alloying with Elements Gadolinium and Zinc for Orthopedic Implant **Applications**

Dong Bian, <sup>†</sup> Jiuxu Deng, <sup>‡</sup> Nan Li, <sup>†</sup> Xiao Chu, <sup>§</sup> Yang Liu, <sup>†</sup> Wenting Li, <sup>†</sup> Hong Cai, <sup>||</sup> Peng Xiu, <sup>||</sup> Yu Zhang, <sup>§</sup> Zhenpeng Guan, <sup>⊥</sup> Yufeng Zheng, <sup>\*,†</sup> Yuhui Kou, <sup>‡</sup> Baoguo Jiang, <sup>\*,‡</sup> and Rongshi Chen\*, <sup>#</sup>

Supporting Information

ABSTRACT: Ternary magnesium alloys with low combined addition of elements gadolinium and zinc were developed in the present work, with their microstructures, mechanical properties, in vitro degradation behaviors, and cytotoxicity being systematically studied. Furthermore, the Mg-1.8Zn-0.2Gd alloy, with the best in vitro performance, was implanted into Sprague Dawley rats to examine its in vivo degradation performance for up to 6 months. It was found that Mg-1.8Zn-0.2Gd, composed of a single  $\alpha$ -Mg phase, owned excellent strength and toughness that were comparable to the CE marked MAGNEZIX, the mischmetal added Mg alloy. Owing to the uniform single-phased microstructure, the degradation rate of this alloy was around 0.12 mm/y measured by electrochemical testing, which was comparable to high purity magnesium. Moreover, the Mg-1.8Zn-0.2Gd alloy exhibited no cytotoxicity to L929, MG63, and VSMC cells. In vivo degradation characterized by micro-



computed tomography revealed that the Mg-1.8Zn-0.2Gd implant could maintain structural integrity in the first 2 months, and serious degradation could be observed after 6 months. A remarkable 100% survival rate of experimental animals was observed with no negative effects on bone tissues. The implant and the surrounding bone were well integrated within 2 months, implying good biocompatibility and osteoconductivity of the experimental alloy. On the basis of the above findings, the feasibility of Mg-Zn-Gd alloys for use as orthopedic implants was systematically discussed. This study provides a new strategy for development of high-performance Mg-rare earth (RE)-based alloys with superior mechanical properties and corrosion resistance while effectively avoiding the possible standing toxic effect of RE elements.

KEYWORDS: Mg-Zn-Gd alloy, rare earth, biodegradability, biocompatibility, osseointegration

## 1. INTRODUCTION

Magnesium-based biodegradable metals have recently received increasing attention because of their acceptable biodegradability, good cytocompatibility, unique antibacterial properties, and superior performance of osseointegration.<sup>1-4</sup> For orthopedic implant applications, the stress-shielding effect can be well eliminated/decreased, as degradable magnesium alloy bone implants share a similar specific density and Young's modulus with the human bone. 5,6 In addition, Mg is an essential element for human health, and it can promote new bone formation. 7-10

Industrial WE43 magnesium alloy series (W represents yttrium and E refers to the mischmetal) were referred during the research and development of biomedical magnesium alloys. The motivation lied in their excellent performances in the industry, that is, decent mechanical properties and good corrosion resistance. For medical devices used for the bone, magnesium-based alloy compression screw (MAGNEZIX, Syntellix AG) was given the CE mark in 2013 as the first, class III medical device made of Mg alloys. 11 Its material composition was chemically similar to the commercial WE43

Received: October 12, 2017 Accepted: January 9, 2018 Published: January 9, 2018

<sup>&</sup>lt;sup>†</sup>Department of Materials Science and Engineering, College of Engineering, Peking University, Beijing 100871, China

<sup>&</sup>lt;sup>‡</sup>Department of Trauma and Orthopedics and <sup>⊥</sup>Arthritis Clinic & Research Center, Peking University People's Hospital, Beijing 100044, China

Department of Orthopedics, Guangdong Key Lab of Orthopaedic Technology and Implant Materials, Guangzhou General Hospital of Guangzhou Military Command, Guangzhou 510010, China

Department of Orthopedics, Peking University Third Hospital, Beijing 100191, China

<sup>&</sup>lt;sup>#</sup>The Group of Magnesium Alloys and Their Applications, Institute of Metal Research, Chinese Academy of Sciences, Shenyang 110016, China

Table 1. Mechanical Properties of Gd-Containing Magnesium Alloys Compared to those of Pure Magnesium and Commercial WE43 Alloy Dedicated for Structural Applications or for Biomedical Purposes<sup>a</sup>

			tensile mechanical property				
material	working condition	target application	TYS (MPa)	UTS (MPa)	elongation (%)	references	
high purity magnesium	as-extruded	biomedical	149	199	8.1	15	
WE43	as-extruded	biomedical	217	298	21.7	16	
Elektron WE43	as-extruded-T5	industrial	195	303	6	17	
Mg-15Gd	as-cast + artificial aging	biomedical	201	251	0.7	18	
Mg-2Gd-1Zn	as-rolled	industrial	130	233	40.3	19	
Mg-3Gd-1Zn	as-rolled	industrial	131	220	40.3	19	
Mg-11Gd-1Zn	as-extruded-T6	industrial	235	416	7.2	20	
$Mg_{96.5}Zn_1Gd_{2.5}$	as-extruded	industrial	345	>370	6.9	21	
Mg-14Gd-0.5Zr	combined extrusion + rolling + aging	industrial	445	482	2.0	22	
Mg-11.8Gd-1.9Er-0.4Zr	repeated plastic working process + hot extrusion	industrial	455	500	12.0	23	
Mg-8.2Gd-3.8Y-1.0Zn-0.4Zr	rolling + aging	industrial	426	517	4.5	24	
<sup>a</sup> T6, T5: peak-aged.							

magnesium alloy. <sup>12</sup> Also, the first clinically proven magnesium-based biodegradable stent (Magmaris, BIOTRONIK, Berlin, Germany) received the CE mark approval in 2016, and the material design was also the modified WE43 magnesium alloy series. <sup>13,14</sup> The negative concern about these alloys is about the long-term biosafety of the mischmetal elements, including the body's metabolism on these metal ions and their possible accumulation in the organs.

Apart from the WE series alloys, gadolinium (Gd)-containing magnesium alloys are another kind of material, which own the most promising ultrahigh strength and very good thermal stability. Recent studies on Mg–Gd-based alloys revealed that they exhibit excellent strength, toughness, and formability, as depicted in Table 1.

Gadolinium is a ductile rare earth (RE) metal, which possesses unusual metallurgic properties. The maximum solubility of Gd in Mg is 23.49 wt %, which is much higher than those of the commonly used RE yttrium (Y, 11.4 wt %) and neodymium (Nd, 3.6 wt %). Besides, its solubility dramatically reduces with decreasing temperature, which means the mechanical properties of Mg-Gd based alloys can be adjusted in a wide range through solid solution and aging strengthening. 18 From the perspective of corrosion, introduction of Gd into magnesium can generally slow down its corrosion. This is mainly attributed to the so-called "scavenger effect" of RE on impurities (Ni, Fe, or Cu). Moreover, Gd incorporated into the corrosion product layer is also beneficial to the film compactness and stability, thus protecting the matrix.<sup>26</sup> The superior combination of mechanical properties and corrosion resistance in Mg-Gd-based alloys makes them promising candidates for future biodegradable metals.

Element Gd has no known native biological role, and its biocompatibility is still controversial. <sup>27,28</sup> Although the free Gd ion was reported to be toxic, different Gd-chelated agents have been approved for use as magnetic resonance imaging contrast agents for a long time. <sup>29,30</sup> Some early research has disclosed that the intraperitoneal median lethal dose (LD<sub>50</sub> dose) of GdCl<sub>3</sub> was 550 mg/kg in mice, whereas GdNO<sub>3</sub> induced acute toxicity at the concentration of 300 mg/kg in mice and 230 mg/kg in rats. <sup>28,31</sup> Recent studies found that Gd showed better tolerability for the tumor-derived mouse macrophage cell line and the human umbilical cord perivascular cells. The production of inflammatory markers of Gd was lower than that of Y, and Gd seemed more suitable than Y as an alloying

element in magnesium.<sup>32</sup> In another study, the 100% original extract of Mg–3Gd induced toxicity to MG63 cells. Nevertheless, the 10% extract was reported to increase the alkaline phosphatase activity of MG63 cells, which might promote mineralization, accelerate bone regeneration, and shorten the healing time.<sup>33</sup> Seriously, biocompatibility of Gd-containing biodegradable metals still needs to be clarified.

As a single alloying element, considerable amounts of Gd are needed to achieve sufficient mechanical strength and qualified corrosion resistance. It was reported that up to 10 wt % of Gd in binary Mg—Gd alloys could guarantee a slow degradation velocity. <sup>18,34</sup> Unfortunately, too much Gd addition is harmful to the biocompatibility of materials. <sup>33,35</sup> Excessive release of Gd may cause possible toxic effects, and this deviates from the design criteria of Mg-RE-based biomaterials. <sup>36</sup> According to a recent study, a high Gd-dosed alloy (Mg—10Gd) disturbed the bone remodeling, and striking adverse results about the Gd accumulation in the main organs of Sprague Dawley rats (SD-rats) was reported. <sup>35</sup>

To maintain the superior properties of Mg–Gd-based alloys while eliminating the possible toxic effects of overdosed Gd addition, another supplementary alloying element is needed. Zinc (Zn) is one of the most abundant essential metal elements in the human body, and it has been proven to be beneficial for the mechanical property and corrosion resistance of magnesium. Mg–Zn–Gd ternary alloys have already showed promising high strength–toughness properties, as revealed in Table 1. Accordingly, Zn was chosen to be the second alloying element. For toxicity and corrosion concerns, the Zn content should also be strictly controlled because Zn<sup>2+</sup> at a high concentration is detrimental to cell differentiation and mineralization. Sp Zn content should be limited to 4 wt % to achieve the best maximum strength and elongation.

On the basis of the general consideration of elemental toxicity, mechanical property, and corrosion resistance, three magnesium alloys with a low combined addition of Gd and Zn were designed and fabricated in the present work. The total alloying addition was restricted to no more than 3 wt %. The actual composition selection was based on our previous experience on this Mg–Zn–Gd alloy system. At those typical compositions, good combinations of strength and toughness could be possibly obtained after rolling. We expect that these alloys could own decent mechanical properties and proper corrosion resistance (retaining the good performances of Mg-

RE alloys) while exhibiting good biocompatibility by reducing the RE content and total alloy elements. The feasibility of these alloys to be used as orthopedic applications was systematically investigated, mainly focusing on the microstructure, mechanical property, corrosion behavior, and in vitro biocompatibility. On the basis of the in vitro results, Mg-1.8Zn-0.2Gd alloy was chosen as the experimental material to conduct in vivo experiments in SD-rats because it owned the best combination of mechanical properties, corrosion resistance, and cytocompatibility. In vivo degradation of the implant was characterized by the micro-computed tomography (CT) analysis, and tissue responses were examined by hard tissue slicing. Eventually, the feasibility of this alloy system to be used as orthopedic implants was comprehensively discussed.

#### 2. EXPERIMENTAL DETAILS

2.1. Materials and Specimen Preparation. Cast billets were prepared with 99.9 wt % Mg, 99.9 wt % Zn, and 99.95 wt % Gd through resistance melting under the protection of a mixed gas atmosphere of SF<sub>6</sub> (1 vol %) and CO<sub>2</sub> (99 vol %). Afterward, they were rolled into thin plates with a final thickness of 2 mm. Details about the preparation procedures can be found in our previous work.<sup>40</sup> Because high purity magnesium (HP-Mg) owns excellent corrosion resistance and biocompatibility, 28 a commercial HP-Mg (as-rolled, 99.99 wt %, DongGuan EONTEC Co., Ltd, China) was adopted as a control material. Nominal and actual compositions of the materials are listed in Table 2. Tensile specimens were machined parallel to the

Table 2. Chemical Compositions of the Experimental Materials Measured by Inductively Coupled Plasma Optical **Emission Spectroscopy (Agilent)** 

material	Zn (wt %)	Gd (wt %)	Mg (wt %)
HP-Mg			99.99
Mg-1.0Zn-2.0Gd	1.04	2.15	bal.
Mg-1.8Zn-0.2Gd	1.81	0.18	bal.
Mg-1.8Zn-0.8Gd	1.85	0.75	bal.

rolling direction according to ASTM-E8-04. 41 Specimens were cut into 10 mm × 10 mm slices for microstructural characterization and in vitro evaluations. Cylindrical rods with a diameter of 0.8 mm were also machined parallel to the rolling direction for the in vivo test. Specimens were mechanically polished with SiC abrasive papers from 400 grit to 2000 grit gradually.

2.2. Microstructural Characterization. Specimens for microstructural observation were further polished with a 5  $\mu$ m diamond polishing paste into a mirrorlike surface. After being etched in 4% nitric acid alcohol solution, the samples were observed under an optical microscope (Leica DM2500, Germany) and a scanning electron microscope (Hitachi S-4800, Japan) equipped with an energy dispersive spectrometer. An X-ray diffractometer (Rigaku DMAX 2400, Japan) was employed to identify the constituent phases using Cu  $K\alpha$  radiation at a scan rate of 4°/min, operated at 40 kV and 100 mA. Samples for transmission electron microscopy (TEM, JEM-2100F, Japan) observation were cut into 50 nm-thick flakes on an ultramicrotome (EM UC6, Leica) and preserved in vacuum before observation. Elemental distribution in the microregions and selected area electron diffraction (SAED) were performed to help identify the constituent phases.

2.3. Mechanical Test. Tensile tests were performed at a crosshead speed of 1 mm/min on a universal material testing machine (Instron 5969, USA) at an ambient temperature. Three measurements were taken for each material. The stress at which 0.2% plastic deformation occurs was defined as tensile yield stress (TYS). Stress at the highest point of the stress-strain curve was the ultimate tensile strength (UTS).

Microhardness test was carried out on a digital microhardness tester (HMV-2T, Shimadzu, Japan) with a load of 49.3 mN and a holding time of 15 s. Eight measurements were performed for each alloy at random sites far from each other.

2.4. Electrochemical Test. Electrochemical measurements were carried out in a three-electrode cell system by using a platinum foil as the counter electrode, a saturated calomel electrode (SCE) as the reference electrode, and experimental materials with an exposed area of 0.45 cm<sup>2</sup> as the working electrode. The test was conducted in Hank's solution on an electrochemical workstation (PGSTAT 302N, Metrohm Autolab). The composition of Hank's solution can be found elsewhere. 42 Open circuit potential (OCP) was continuously monitored for 3600 s. Electrochemical impedance spectroscopy (EIS) was measured from 100 kHz to 10 mHz at the OCP value. Then, the potentiodynamic polarization measurement was conducted from -0.5 to 1 V (vs SCE) at a scan rate of 0.001 V/s. Three duplicate samples for each material were tested for statistical analysis.

**2.5. Immersion Test.** Different from the electrochemical corrosion test, immersion tests were performed to observe the long-term corrosion behaviors. Samples were immersed in Hank's solution at 37 ± 1 °C, according to ASTM-G31-72, 43 with an exposure ratio of 20 mL/cm<sup>2</sup>. The pH value during immersion was monitored, and the volume of emerged hydrogen was recorded. The evolved hydrogen was collected through an inverted funnel and guided into a calibrated burette; then its volume was recorded in accordance with ref 44. The ion concentration of the corrosion medium after immersion was measured by using an inductively coupled plasma mass spectrometer (DRC-II, PerkinElmer). Surface morphology after immersion was characterized using scanning electron microscopy (SEM). Corrosion products on the sample surface were characterized by X-ray diffraction (XRD) and energy dispersive spectroscopy (EDS) analysis. Weight loss was also measured after removing the corrosion products in chromic acid, according to ASTM-G1-90. 45 Corrosion rate was calculated from the weight loss by using the following equation, CR =  $3.65\Delta W/\rho$ ; <sup>46</sup> where  $\Delta W$  is the metal weight loss rate (mg/cm<sup>2</sup>/d) and  $\rho$  is the metal density (g/cm<sup>3</sup>). At least three samples were tested in each group.

2.6. Cytotoxicity. In the indirect cell assay, four kinds of cells, namely murine fibroblast cells (L929), human osteosarcoma cells (MG63), vascular smooth muscle cells (VSMC), and human umbilical vein endothelial cells (ECV304), were used. MG63 is a bone-related cell line and fibroblast is related to the fibrosis of the orthopedic implant. These two common cell lines are suitable for cytotoxicity evaluation of materials, which are proposed to be used in the bone environment. Ions derived from the magnesium-based implant during in vivo degradation will enter into blood circulation and interact with vascular endothelial cells and smooth muscle cells. So, VSMC and ECV304 cells were also included in the cytotoxicity evaluation. All cells were cultured under standard cell culture conditions at 37 °C in a humidified atmosphere of 5% CO<sub>2</sub>. The cells were cultured in Dulbecco's modified Eagle's medium (DMEM) supplied with 10% fetal bovine serum, 100 U/mL penicillin, and 100  $\mu$ g/mg streptomycin.

Alloy extracts were prepared by using a serum-free DMEM with an extraction ratio of 1 cm<sup>2</sup>/mL in a humidified atmosphere with 5% CO<sub>2</sub> at 37 °C for 72 h. The original 100% extracts were diluted into 50 and 10% concentrations with DMEM before use. Ion concentrations and pH values of the extracts were measured as well.

Methylthiazol tetrazolium (MTT) assay was adopted to evaluate the cytotoxicity of the alloy extracts according to ISO 10993-5:2009(E). Cells were seeded onto 96-well culture plates at a density of  $3-5 \times 10^4$ mL<sup>-1</sup> and incubated for 24 h to allow attachment. Then, the medium was replaced by alloy extracts (100, 50, and 10%), with normal culture medium as the negative control and medium supplied with 10% dimethylsulfoxide as the positive control. After incubating for 1, 3, and 5 days, 10  $\mu$ L of MTT was added into each well for 4 h. The extracts were replaced by fresh medium before the addition of MTT. Thereafter, 100  $\mu$ L of formazan solubilizing solution (10% sodium dodecyl sulfate in 0.01 M HCl) was added to each well and left overnight in an incubator. The spectrophotometric absorbance of each

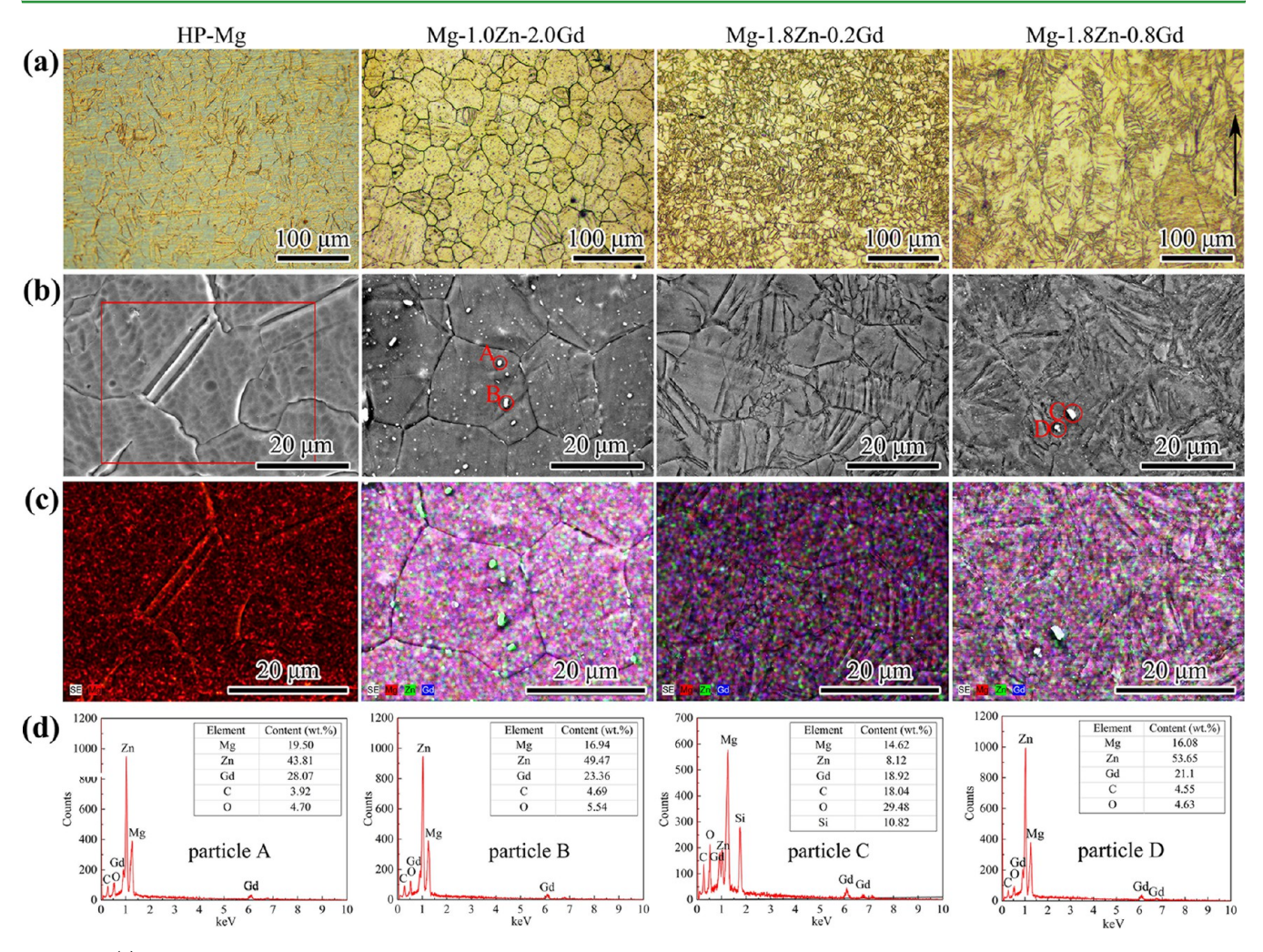


Figure 1. (a) Microstructures of HP-Mg and Mg–Zn–Gd alloys observed under an optical microscope; black arrow indicates the elongated direction of grains in the Mg–1.8Zn–0.8Gd alloy; (b) microstructures under SEM; (c) elemental distribution on the sample surface corresponding to the selected areas in (b); (d) EDS results corresponding to particles in (b). High contents of Si, C, and O in particle C are contaminations derived from the polishing process.

well was measured by using a microplate reader (Bio-Rad 680) at 570 nm with a reference wavelength of 630 nm.

LIVE/DEAD cell assay was performed according to the manufacturer's protocol (LIVE/DEAD staining kit, BestBio). Briefly, the cells were cultured in 48-well culture plates with alloy extracts (details about the cell culture are described before in the MTT assay), and at the end of the incubation period, the medium was removed and 200  $\mu$ L of the staining reagent was added after the cells were gently washed with phosphate-buffered solution (PBS). The staining reagent was removed after incubation for 30 min at 37 °C in darkness. Then, 100  $\mu$ L of normal culture medium was added into the well after the cells were gently washed with PBS. The cells were then photographed under a fluorescence microscope (Leica DMI4000B, Germany). Cell morphology was captured at the same site in individual plate wells to make a reliable and valid comparison.

**2.7. Animal Test.** *2.7.1. Animal Model and Surgery.* Eighteen female SD-rats weighing 200–250 g were provided by the Laboratory Animal Center of Peking University People's Hospital (SPF level, animal use permit no. SYXK (jing) 2011-0010). The rats were anaesthetized by intraperitoneal injection of pentobarbital sodium at a dosage of 30 mg/kg. Operation sites around the left knee joint were shaved and sterilized, followed by decortication. A predrilled hole, 0.8 mm in diameter, was made on the lower edge of the tibial plateau by using an orthopedic drill. A Mg–1.8Zn–0.2Gd pin (Φ 0.8 mm) was inserted into the predrilled hole on the left tibia. Following insertion, the pin was cut at the tibial cortical surface. The implant length varied

between 7 and 9 mm depending on the actual implantation position and animal bone size. The normal right tibia without implantation was used as the control. After surgery, the animals were kept under normal conditions and provided with plenty of food and water. The anesthetic, surgical, and postoperative care protocols were examined by the Ethics Committee of Peking University People's Hospital and their requirements were fulfilled.

2.7.2. Postoperative Observation, Micro-CT, and Histological Evaluation. All animals were clinically examined for general condition and in particular for significant signs of lameness, infection, subcutaneous emphysema formation, and loss of appetite. Six animals were sacrificed by overdosage anesthesia at each time point post operation (1, 2, and 6 months). Rat tibias were retrieved and scanned by using a self-built micro-CT device at a spatial resolution of 35  $\mu$ m. Three-dimensional (3D) reconstruction was performed using Amira software (Amira 5.4.1, Visage Imaging). Bones with magnesium implants were fixed in 10% formalin and dehydrated in gradient ethanol/distilled water mixtures. Then, they were embedded in methacrylate and sectioned into 150  $\mu m$  slices on an EXAKT system (EXAKT Apparatebau, Norderstedt, Germany). The hard tissue sections were further grounded to  $50-80~\mu m$  before staining with hematoxylin-eosin (H&E) or toluidine blue (Guge Biological Technology Co., Ltd.). Details about the hard tissue slicing process can be found in our previous work.4

**2.8. Statistical Analysis.** Data in this work are expressed as means  $\pm$  standard deviation. Statistical analysis was performed with SPSS 18.0

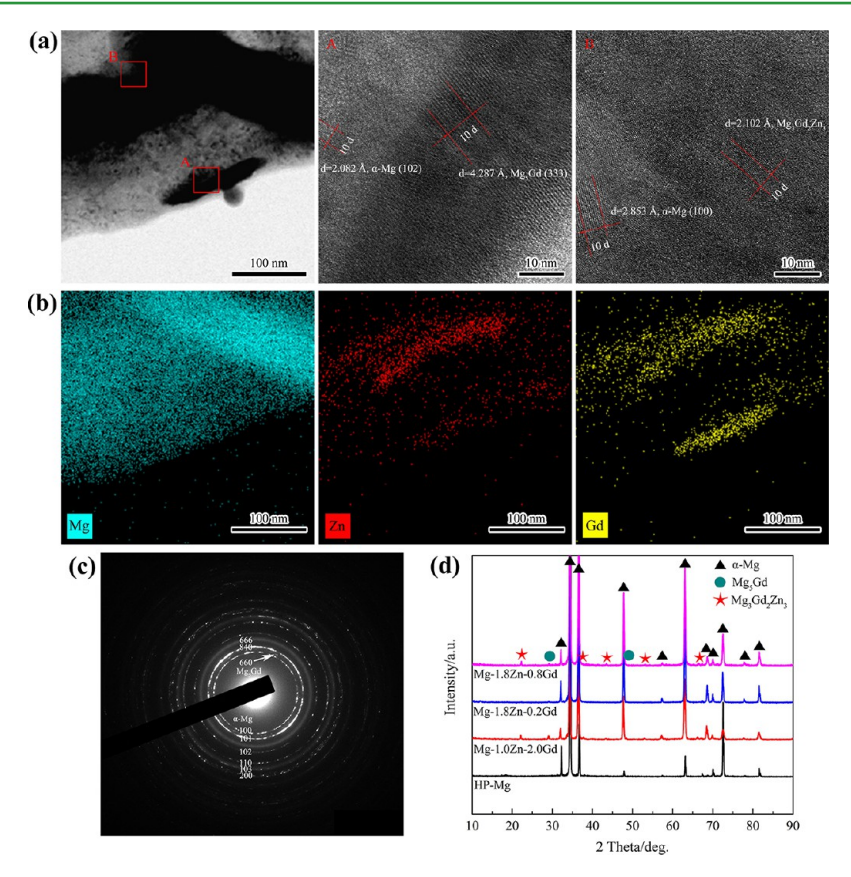


Figure 2. (a) Typical second phases found in Mg-1.0Zn-2.0Gd and Mg-1.8Zn-0.8Gd under TEM (bright-field HRTEM images were taken at specific sites marked with letter A and B); (b) elemental (Mg, Zn, and Gd) distribution analysis corresponding to those second-phase particles in (a); (c) selected area diffraction image showing the presence of the α-Mg matrix and second phases; (d) XRD patterns of the experimental materials.

software (SPSS Inc., Chicago, USA). Differences between groups were analyzed using one-way analysis of variance, followed by the Tukey test. A p-value < 0.05 was considered a statistically significant difference.

#### 3. RESULTS

**3.1. Microstructure.** Figure 1 displays the microstructures and the corresponding elemental analysis of the experimental materials. HP-Mg was composed of a single  $\alpha$ -Mg phased microstructure with a number of twins inside the equiaxed grains. Mg-1.8Zn-0.2Gd owned the finest grains with abundant twins inside. Mg-1.0Zn-2.0Gd exhibited a fully recrystallized microstructure with only limited twins in the interior of the equiaxed grains. In the Mg-1.8Zn-0.8Gd alloy, elongated grains could still be found, and the black arrow in Figure 1a indicates the elongated direction. Some particles with size less than 5 µm could be found in Mg-1.0Zn-2.0Gd and Mg-1.8Zn-0.8Gd. Much more particles in the Mg-1.0Zn-2.0Gd alloy were in accordance with its highest content of total alloying elements among the three alloys. These particles were rich in Zn and Gd, as revealed by area scanning and point scanning in the EDS analysis (Figure 1c,d).

Typical microstructures of Mg-1.0Zn-2.0Gd and Mg-1.8Zn-0.8Gd using TEM are presented in Figure 2a. Because the microstructures of the two alloys are quite similar under TEM, only one typical microstructural image is displayed here. Second phases rich in Gd (particle A) or Zn and Gd (particle B) could be detected, as depicted in Figure 2b. High-resolution transmission electron microscopy (HRTEM) images of typical areas in particle A and particle B revealed that their interplanar

spacings (d) are 0.4287 and 0.2102 nm, respectively. In the SAED patterns, besides the diffraction rings of the  $\alpha$ -Mg matrix, several rings corresponding to the second phases could also be observed. With the help of the XRD analysis, besides the  $\alpha$ -Mg matrix, Mg<sub>5</sub>Gd and Mg<sub>3</sub>Gd<sub>2</sub>Zn<sub>3</sub> phases were also detected in Mg-1.0Zn-2.0Gd and Mg-1.8Zn-0.8Gd alloys, as shown in Figure 2d. On the basis of the above analysis, particle A could be identified as the Mg<sub>5</sub>Gd phase and particle B should correspond to the Mg<sub>3</sub>Gd<sub>2</sub>Zn<sub>3</sub> phase.

3.2. Mechanical Property. Figure 3 displays the mechanical behaviors of Mg-Zn-Gd alloys with the as-rolled HP-Mg as the control. Compared to the as-rolled HP-Mg, Mg-1.8Zn-0.8Gd and Mg-1.8Zn-0.2Gd exhibited significantly improved TYS and UTS with comparable tensile elongation. On the contrary, Mg-1.0Zn-2.0Gd showed a significant higher tensile elongation (>30%) while at the same strength level of HP-Mg, as shown in Figure 3a,b. The microhardness followed a similar trend with the UTS, as depicted in Figure 3c. Not much difference could be found on the tensile fracture morphologies among HP-Mg, Mg-1.8Zn-0.2Gd, and Mg-1.8Zn-0.8Gd, all showing a composite fracture mode with limited dimples and tearing edges. However, a ductile fracture morphology with quite abundant deep dimples and tearing ridges was observed on Mg-1.0Zn-2.0Gd, in good agreement with its largest elongation among all experimental materials. In general, Mg-1.8Zn-0.2Gd and Mg-1.8Zn-0.8Gd alloys exhibited a favorable combination of strength and toughness, with UTS around 300 MPa and elongation higher than 14%.

**3.3.** In Vitro Degradation. 3.3.1. Electrochemical Corrosion Behavior. During the corrosion process, a protective/

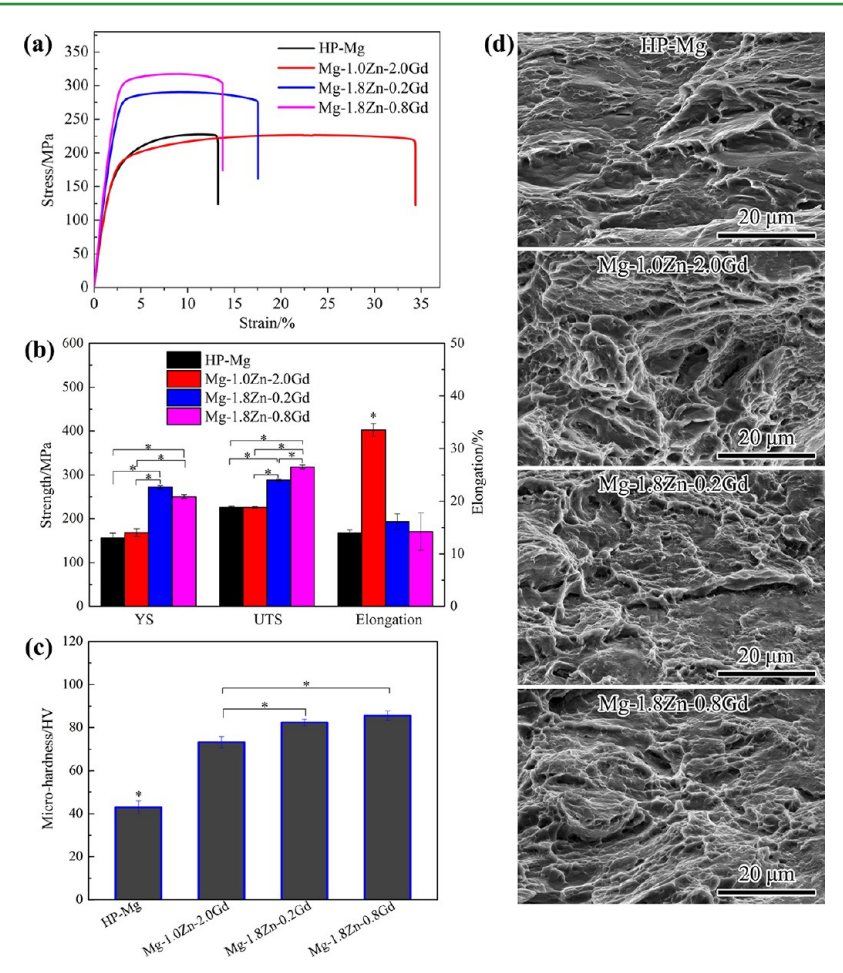


Figure 3. Mechanical performances of Mg–Zn–Gd alloys with as-rolled HP-Mg as the control: (a) typical stress–strain curves, (b) mechanical data, (c) microhardness, and (d) their corresponding fracture morphologies. \*p-value < 0.01.

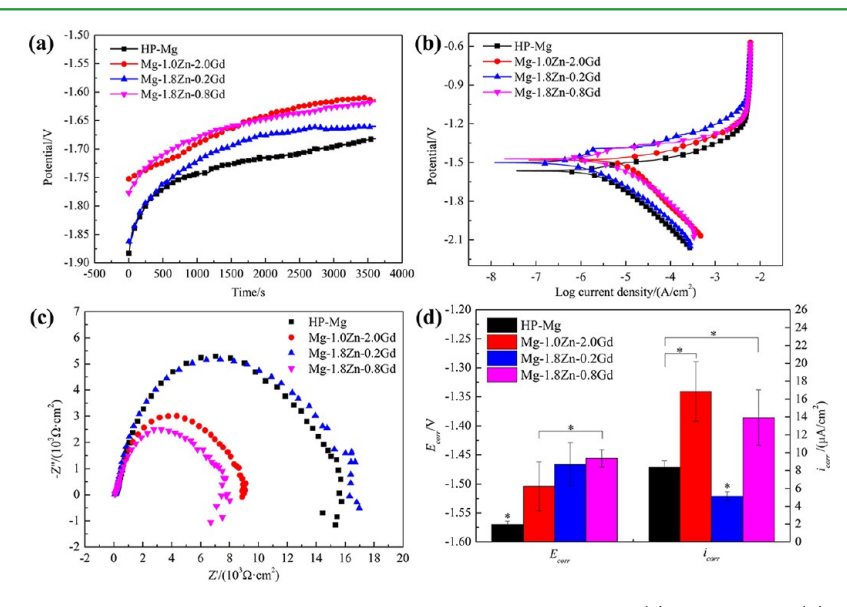


Figure 4. Electrochemical corrosion behaviors of the experimental materials in Hank's solution: (a) OCP curves, (b) potentiodynamic polarization curves, (c) Nyquist plots, and (d) electrochemical data illustrated in the histogram.  $E_{corr}$  represents the corrosion potential and  $i_{corr}$  represents the corrosion current density.

partially protective  $Mg(OH)_2$  layer was formed with the dissolution of magnesium, leading to the OCP increase. From the perspective of thermodynamics, a higher OCP value meant the matrix was more stable. OCP values of Mg-Zn-Gd alloys

were all improved compared to that of HP-Mg, as shown in Figure 4a. Mg-1.0Zn-2.0Gd and Mg-1.8Zn-0.8Gd presented more positive and more stable OCP values compared to HP-Mg and Mg-1.8Zn-0.2Gd.

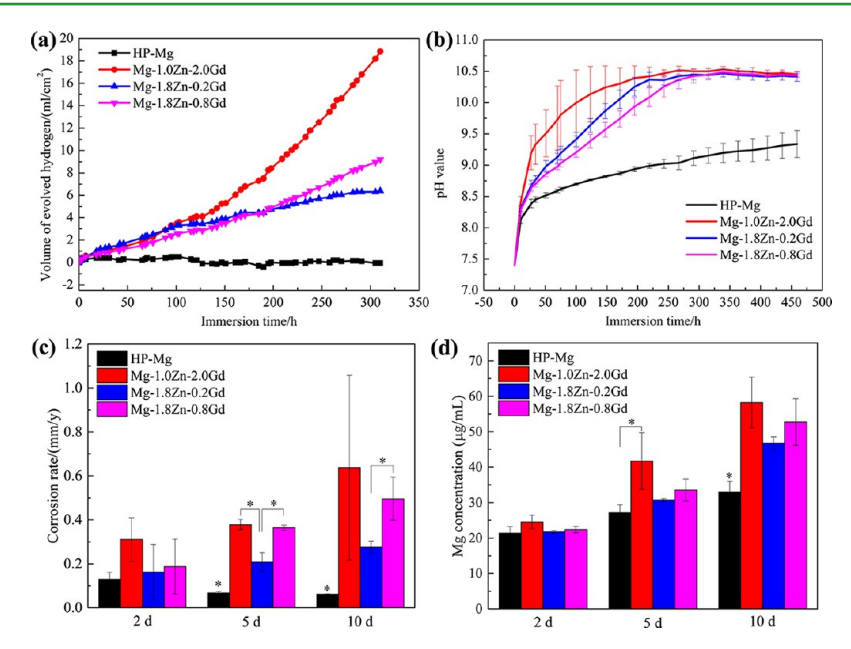


Figure 5. Immersion corrosion behaviors in Hank's solution at 37 °C: (a) volume of the evolved hydrogen, (b) pH monitoring during static immersion, (c) corrosion rate calculated from the weight loss, and (d) ion-releasing behavior during immersion.

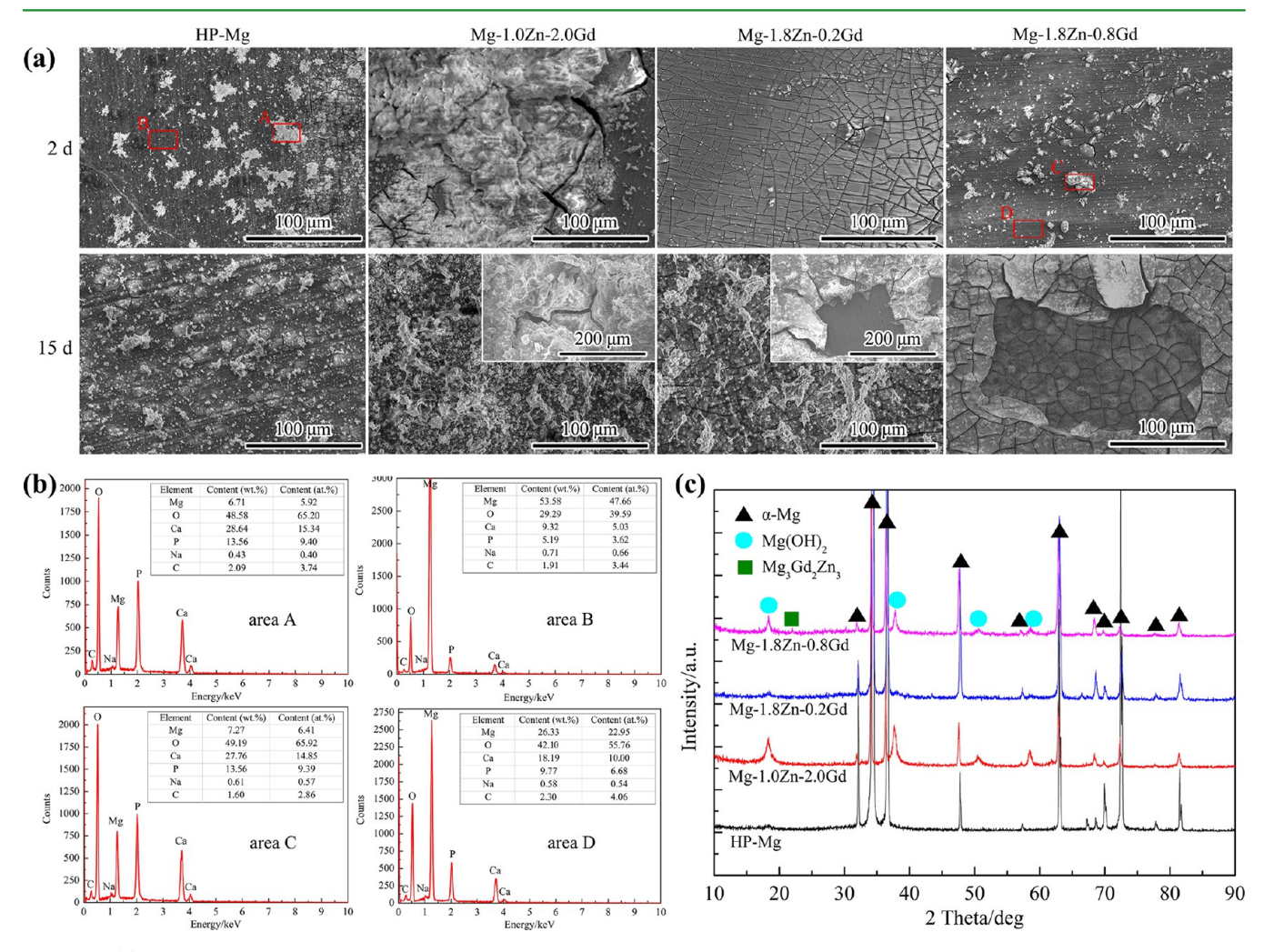


Figure 6. (a) Typical corrosion morphologies of the experimental materials after immersion for 2 and 15 days (insets showing the localized corrosion and peeling-off of the corrosion product layer on Mg-1.0Zn-2.0Gd and Mg-1.8Zn-0.2Gd alloys after 15 day-immersion, respectively); (b) EDS results of specific areas in (a); (c) XRD patterns of samples after 15 day-immersion.

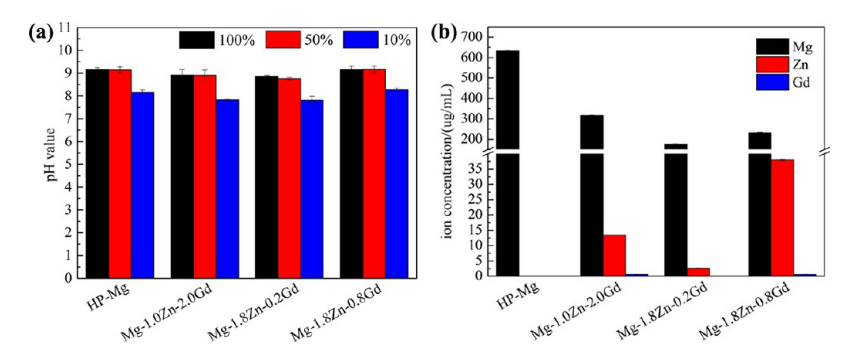


Figure 7. Characterization of the extract media: (a) pH value and (b) magnesium and alloying element concentrations in the extracts.

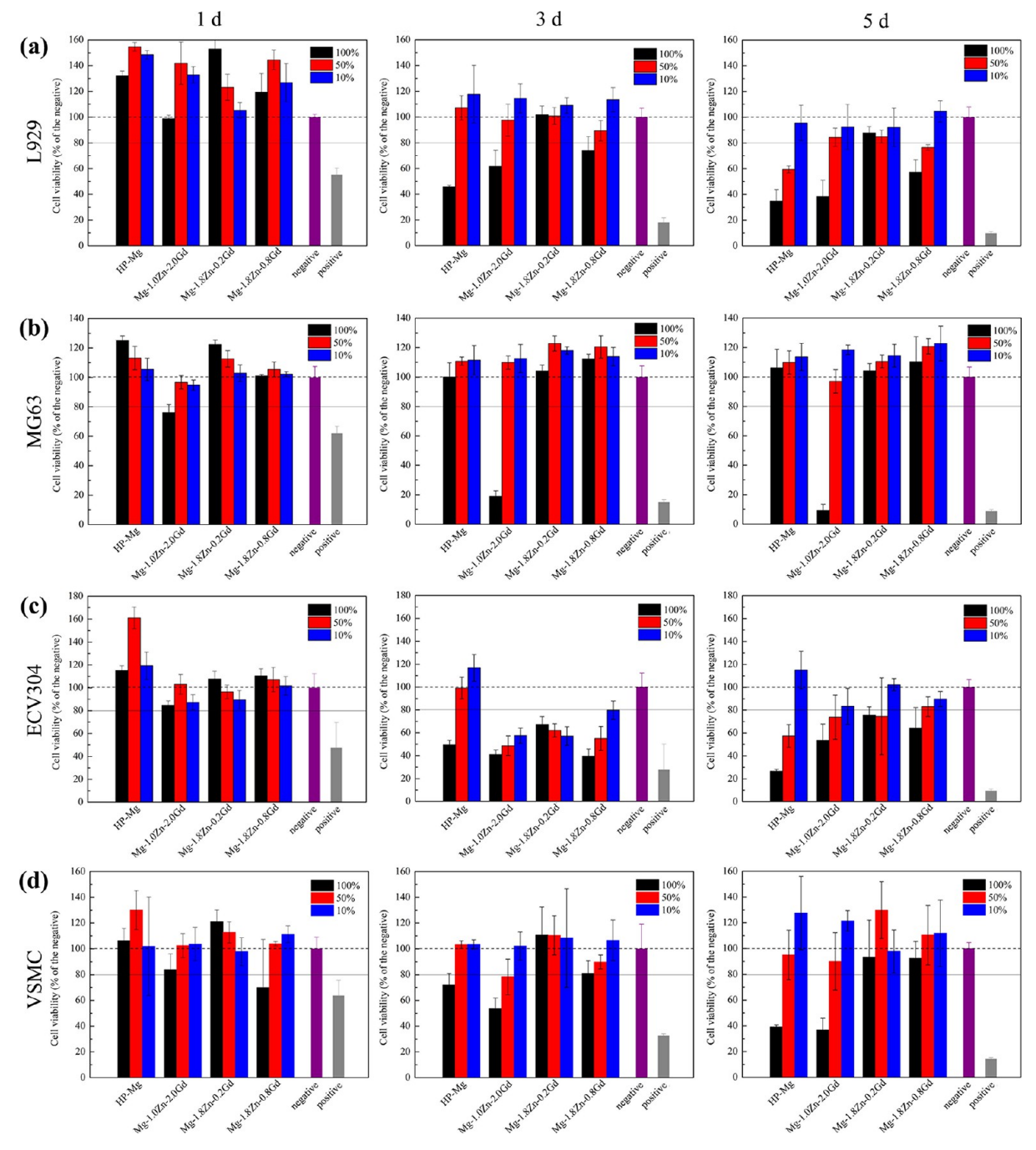


Figure 8. Cytotoxicity tests of (a) L929, (b) MG63, (c) ECV304, and (d) VSMC cells in HP-Mg and Mg-Zn-Gd alloy extracts.

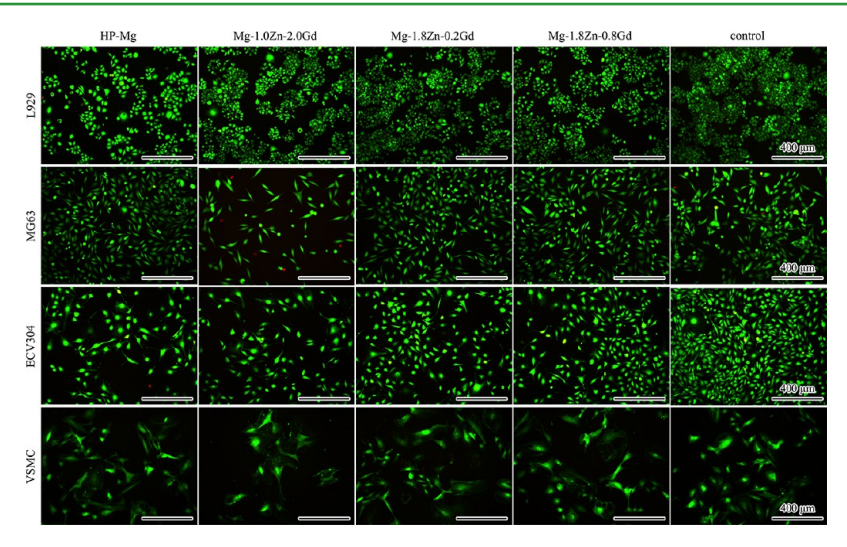


Figure 9. LIVE/DEAD staining of various cells after culturing in HP-Mg and Mg-Zn-Gd alloy extracts (100% extract, without dilution) for 3 days, with normal culture medium as the control (red represents dead cells and green represents live cells).

The cathodic polarization current reflected the severity of hydrogen evolution reaction on the platinum electrode. HP-Mg and Mg-1.8Zn-0.2Gd exhibited a significantly lower cathodic current density compared with Mg-1.0Zn-2.0Gd and Mg-1.8Zn-0.8Gd, suggesting better corrosion resistance. It is well-known that a larger loop in the EIS spectra (Nyquist plots) means better corrosion resistance, <sup>49</sup> and hence HP-Mg and Mg-1.8Zn-0.2Gd were more anticorrosive than Mg-1.0Zn-2.0Gd and Mg-1.8Zn-0.8Gd, corresponding to the polarization curves, as illustrated in Figure 4b,c.

Electrochemical corrosion parameters, including corrosion potential  $(E_{\rm corr})$  and corrosion current density  $(i_{\rm corr})$ , derived directly from the polarization plots by using Tafel region extrapolation are listed in Figure 4d.  $E_{\rm corr}$  values of all three Mg–Zn–Gd alloys were apparently higher than that of HP-Mg, and furthermore, Mg–1.8Zn–0.2Gd exhibited even a lower corrosion rate than HP-Mg.

3.3.2. Immersion Corrosion Behavior. Figure 5 displays the volume of evolved hydrogen, pH value variation, corrosion rate, and ion-releasing behavior with immersion time. In the first few hours, there was no obvious difference of evolved hydrogen and pH value among all experimental materials. Afterward, the corrosion behaviors differed with different alloys. During the whole immersion period, HP-Mg had the least hydrogen evolution and the slowest pH increase, implying the best corrosion resistance. The corrosion behaviors of Mg-1.8Zn-0.2Gd and Mg-1.8Zn-0.8Gd were quite similar within 200 h, however, a slight increase in the hydrogen volume was found in Mg-1.8Zn-0.8Gd afterward. Mg-1.0Zn-2.0Gd exhibited constantly aggravated corrosion with prolonged immersion time. Corrosion rates calculated from the weight loss revealed that HP-Mg owned the best corrosion resistance; meanwhile, corrosion of Mg-1.8Zn-0.2Gd was at a relatively low level, < 0.28 mm/y.

The Mg releasing behavior during immersion showed a variation trend similar to that of the weight loss, as depicted in Figure 5c,d. Ion concentration (Mg<sup>2+</sup>) increased with immersion time, suggesting the continuous dissolution of all samples. HP-Mg exhibited the lowest corrosion rate as it released the least amount of Mg. Mg-1.8Zn-0.2Gd was more anticorrosive than the other two Mg-Zn-Gd alloys. Concentrations of Zn, Gd, Ca, and P in the corrosion medium

are displayed in the Supporting Information, Figure S1. Briefly, Gd concentration continuously increased with prolonged immersion time, yet Ca and P concentrations showed an opposite trend. There was no apparent regular pattern in the Zn concentration variation, possibly due to its complex dissolution and deposition on the corrosion product layer with time. The faster a material was corroded, lower Ca and P concentrations could be detected in its corrosion medium. The decreasing concentration of Ca and P was closely related to their deposition on the corroded sample surface.

Typical corrosion morphology, surface composition analysis, and phase identification of the corrosion product layer are presented in Figure 6. Corrosion of HP-Mg, Mg-1.8Zn-0.2Gd, and Mg-1.8Zn-0.8Gd were macroscopically homogeneous, nevertheless, severely localized corrosion was found on the Mg-1.0Zn-2.0Gd sample, as depicted in Figure 6a. With increasing immersion time (15 d), peeling-off of the corrosion product could be observed, possibly derived from the dehydration process and thickening of this layer. A corrosion product layer, mainly composed of Mg(OH)<sub>2</sub>, was formed on the sample surface, as shown in Figure 6c. Some white particles/clusters were deposited on this layer, and they were rich in Ca, P, and O. A small amount of C and Na was also detected in the corrosion product layer.

**3.4. Cytotoxicity.** Figure 7 presents the pH values and ion concentrations in the extract media. There was no significant difference in the pH values of the 100% extracts, all approximating to 9. Because of the buffer effect of the medium, pH values only slightly decreased after dilution to 50%. The pH values would be reduced to as low as 7.81 for a further dilution to 10%.  $\rm Mg^{2+}$  releasing during the extraction process could reflect the corrosion rate in DMEM.  $\rm Mg-Zn-Gd$  alloys showed lower corrosion rates compared to HP-Mg.  $\rm Mg-1.8Zn-0.2Gd$  exhibited the lowest  $\rm Mg^{2+}$  concentration, suggesting the best corrosion resistance. In addition, Gd concentration in the  $\rm Mg-1.8Zn-0.2Gd$  extract was well below the minimum detection limit (<0.1  $\mu\rm g/mL$ ) of inductively coupled plasma atomic emission spectroscopy (Leeman).

Cell viability was expressed as a percentage of the optical density of cells cultured in the negative control, as displayed in Figure 8. Except for the 100% Mg-1.0Zn-2.0Gd extract, all remaining extracts improved the L929 cell viability on day 1.

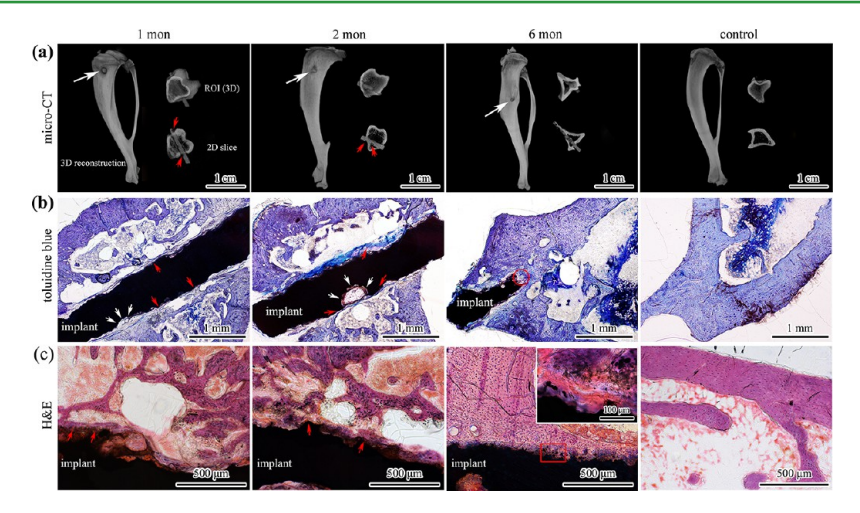


Figure 10. (a)Typical micro-CT characterization of rat tibias after implantation for 1, 2, and 6 months, with normal bone as the control (white arrows indicate the implantation sites and red arrows indicate the signs of localized corrosion. ROI: region of interest); (b,c) typical histological staining of the hard tissue sections with toluidine blue and H&E, respectively. White arrows indicate the site of localized corrosion, and red arrows point out the newly formed bone. The inset in (c) shows some tiny particles or debris derived from the implants in the adjacent bone tissues.

However, L929 cell viability was reduced later on, as shown in Figure 8a. The 100% Mg-1.0Zn-2.0Gd extract led to a significant decrease of MG63 cell viability with increasing culture time. Toxic effects of the Mg-1.0Zn-2.0Gd extract to MG63 cells could be mitigated by dilution. Extracts of HP-Mg, Mg-1.8Zn-0.2Gd, and Mg-1.8Zn-0.8Gd exhibited no cytotoxicity to MG63 cells, all showing high cell viability (>100%). For ECV304 cells, all experimental extracts showed no toxicity on day 1, with cell viability higher than 80%. Cell viability of 10% HP-Mg extract was stabilized in the range of 110–120% during the whole culture period. Cell viability of the three Mg-Zn-Gd alloys decreased to a certain degree on day 3, but it had a certain rise on day 5. The Mg-1.8Zn-0.2Gd extract showed no cytotoxicity to VSMC cells during the whole incubation period. The 100% extracts of HP-Mg and Mg-1.0Zn-2.0Gd both caused a continuous decrease of VSMC cell viability with prolonged culture time.

Cell viability and attachment were also examined through the LIVE/DEAD staining assay, as shown in Figure 9. All four kinds of cells cultured in alloy extracts were well-attached to the well-plate bottom, and their spreading morphologies were similar to those of the normal controls on day 3. Quite limited dead cells (red color) could be randomly observed in all groups and in all kinds of cells. The main difference between the experimental groups and the normal control group was the cell density (number of cells). Specially, L929 cells in the HP-Mg group, MG63 cells in the Mg-1.0Zn-2.0Gd group, and VSMC cells in the Mg-1.0Zn-2.0Gd group were obviously less in number than their own controls. Although the MG63 cell density in the Mg-1.0Zn-2.0Gd extract was lower than its counterparts, a higher proportion of dead cells was still found. After 5 day-culturing, MG63 cells of the Mg-1.0Zn-2.0Gd group was in poor condition, with many dead cells and limited living cells in abnormal morphologies, as shown in the Supporting Information, Figure S2. Dilution of the extract could effectively mitigate the cytotoxicity, and this is also depicted in the Supporting Information, Figure S2. On the basis of the MTT and LIVE/DEAD staining results, it could be basically concluded that cytotoxicity of the extracts was closely related to the inhibition of cell proliferation.

**3.5.** In Vivo Performance. All animals that received implantation survived, and no obvious signs of lameness and

loss of appetite were observed. No infection was found through autopsy and micro-CT examination.

3.5.1. Micro-CT Assessment. In vivo degradation of Mg-Zn-Gd implants was characterized by the micro-CT analysis, as depicted in Figure 10a here. Continuous degradation of the implant could be found and signs of localized corrosion could also be observed, as indicated by red arrows in Figure 10a. Although localized corrosion occurred, the implant was intact with its structure in the first 2 months. After 6 months, only some residual parts of the implant could be detected. In some areas, full degradation of the implant was observed, and the place where the implant was previously held was filled with newly formed bone tissues. Continuous bone-implant osseointegration could also be observed along with implant degradation. In the first month, the implant was surrounded by a low-density circular shadow, as revealed from the micro-CT examination, implying the weak bonding between the bone and the implant. Two months later, the implant was in direct contact with the surrounding bones, as shown in the 3D reconstructions and two-dimensional slices in Figure 10a.

3.5.2. Histological Analysis. Figure 10b,c shows the tissue response adjacent to the Mg-1.8Zn-0.2Gd implant at 1, 2, and 6 months post surgery. Gradual degradation of the Mg-1.8Zn-0.2Gd pin could be observed, and mildly localized corrosion happened, as indicated by the white arrows. In the first 2 months, the implant kept its structural integrity as the degradation continued. However, only some residual parts were found at 6 months. Along with degradation, new bone formation was found closely adjacent to the Mg-1.8Zn-0.2Gd implant, as marked by the red arrows in Figure 10b,c. In specific areas, as marked by a red circle in Figure 10b, the space where the implant previously occupied was replaced by newly formed bones. With prolonged implantation time, better integration between the bone tissues and implants was observed. No abnormality was found with bone tissues surrounding the implant material, showing good histocompatibility.

Bone-implant interfaces were closely related to the osseointegration and bonding strength. Different parts of the implant were located in totally different local environments. Both ends were embedded in the cortical bones while the middle section of the implant was exposed to the bone marrow,

as illustrated in Figure 11a. So, even in the same sample, details at the bone-implant interface differed greatly at different sites.

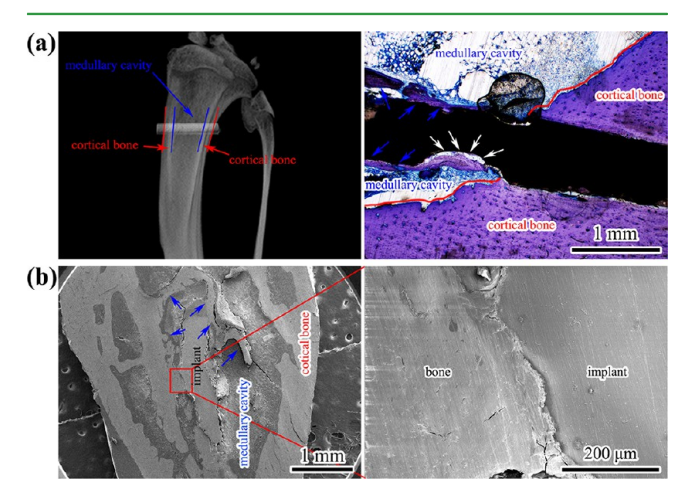


Figure 11. (a) Illustration of the relative locations of different parts of the implant in the bone environment and the corresponding histological observation at 6 months (blue arrows indicate the bones surrounding the implant in the medullary cavity, and white arrows mark the locally corroded site); (b) SEM images showing the newly formed bone tissues surrounding the implant in the medullary cavity and the details at the bone-implant interface (good bonding).

In the cortical zones, the implant was directly integrated with the surrounding bones after 6 months, showing good bonding. In the medullary cavity, some newly formed trabecular bones could be observed surrounding the implant, as indicated by blue arrows in the histological and SEM images. Some of these trabecular bones were directly in contact with the implant while some had a certain distance to the implant. Wherever localized corrosion happened (either in the cortical bone or in the marrow cavity), nonbonding or delayed osseointegration between the bone and implant developed, as marked by the white arrows both in Figures 10b and 11a.

#### 4. DISCUSSION

4.1. Possibility of Using Mg-Zn-Gd Alloys as Orthopedic Implants. 4.1.1. Mechanical Property and Corrosion Resistance. The as-rolled Mg-1.0Zn-2.0Gd exhibited a fully recrystallized microstructure with abundant second-phase particles throughout the matrix. However, the strengths of the Mg-1.0Zn-2.0Gd alloy were similar to those of HP-Mg, showing no obvious solid solution strengthening or precipitation strengthening. The excellent formability of this alloy could be attributed to the nonbasal texture and low texture intensity, as proved in our previous research.<sup>19</sup> No obvious second-phase particles were found in Mg-1.8Zn-0.2Gd both under SEM and TEM. Improved strength of the Mg-1.8Zn-0.2Gd alloy was mainly derived from its fine microstructure accompanied by homogeneous subgrain microstructures (twins could act as barriers in the dislocation slip and thus improve the strength) and solid solution strengthening effect. Precipitations and textures derived from the rolling process also contributed to the mechanical strength of Mg-1.8Zn-0.8Gd. From the perspective of thermodynamics, the combined addition of Gd and Zn into magnesium stabilized the matrix, as confirmed by the OCP improvement. However, the dynamic equilibrium among the alloy matrix, corrosion product layer, and electrolyte determined the corrosion rate. Fast

degradation of Mg-1.0Zn-2.0Gd in Hank's solution should be ascribed to the galvanic corrosion between the  $\alpha$ -Mg matrix and second phases. Besides, drastic galvanic corrosion also led to severely localized corrosion and further increased the corrosion rate. In the Mg-1.8Zn-0.8Gd alloy, second-phase particles were less in amount and smaller in size, and the galvanic corrosion was mitigated. Galvanic effects were greatly depressed or possibly eliminated, as Mg-1.8Zn-0.2Gd was composed of a single  $\alpha$ -Mg phase and galvanic couples could not form.

Impacts of different electrolytes on the corrosion behaviors were also observed in this study. In Hank's solution, HP-Mg exhibited the most impressive corrosion resistance; on the contrary, it owned the highest corrosion rate in DMEM. Compared to DMEM, Hank's solution only contains inorganic salts. The high amount of chloride (Cl-) in Hank's solution leads to high corrosion rates. 50,51 In addition to inorganic salts, DMEM also includes amino acids and vitamins, much closer to the practical physiological condition.<sup>52</sup> Besides, the environment under standard cell culture conditions has a continuous and stable CO<sub>2</sub> supply (HCO<sub>3</sub><sup>-</sup> as a buffer). These components significantly alter the corrosion behaviors probably by protein adsorption on the surface and their involvement in the corrosion process and construction of the corrosion product layer. 53,54 In our study, compositions of the alloy matrix and their dissolution during degradation also have an impact on the corrosion behaviors. The combined addition of Gd and Zn was prone to be beneficial for the corrosion resistance in DMEM.

4.1.2. Cytotoxicity. According to ISO 10993-5, cytotoxicity of biomaterials should be grade 0 or grade 1, which means cell viability should exceed 80%.<sup>47</sup> The released ions and the improved pH value should be responsible for the cytotoxicity of magnesium-based biomaterials. Differences among the alloy extracts mainly lie in their ion concentrations because pH values of the extracts (at the same concentration level) are almost the same. Mg-1.8Zn-0.2Gd exhibited no cytotoxicity to L929, MG63, and VSMC cells because concentrations of Mg, Zn, and Gd were well under their tolerance limits. Tolerance limits varied with different cells as L929, MG63, and VSMC cells showed better tolerance to Mg-Zn-Gd alloy extracts than ECV304 cells.

In the pH range of 7.5–9.0, 63.27  $\mu$ g/mL Mg in the extract exhibited no cytotoxicity to L929 cells, but Mg concentration at 316.34  $\mu$ g/mL induced toxicity. Mg concentration at 632.67 µg/mL did not induce any cytotoxicity to MG63 cells, and the combined ion concentrations of 232.67  $\mu$ g/mL Mg + 38  $\mu$ g/ mL Zn + 0.58  $\mu$ g/mL Gd also had no cytotoxicity. A much higher Mg content in the Mg-1.0Zn-2.0Gd extract should be mainly responsible for the severe toxicity to MG63 cells. Mg concentration at 316.34  $\mu$ g/mL caused cytotoxicity to ECV304 cells, and ECV304 cells might bear the Mg-1.8Zn-0.2Gd and Mg-1.8Zn-0.8Gd extracts with a prolonged culture time. Mg concentration lower than 316.34 µg/mL did not cause cytotoxicity to VSMC cells. However, accompanied with 13.42  $\mu$ g/mL Zn and 0.59  $\mu$ g/mL Gd, even at the same Mg level, obvious cytotoxicity occurred. It can be inferred that cytotoxicity of alloying elements in the extracts interacted with each other, and the tolerance limit of a specific element could be reduced by other elements.

Table 3 lists the performances of our Mg–Zn–Gd alloys compared to those of previously reported binary Mg–Zn and Mg–Gd alloys and also some of the most promising magnesium-based biomaterials in orthopedics. Generally, the

Table 3. Mechanical Properties and Corrosion Rates of Mg-Zn-Gd Alloys Compared to those of Previously Reported Binary Mg-Zn and Mg-Gd Alloys Developed for Biomedical Applications and Also to the Most Promising Magnesium-Based Biomaterials for Orthopedics

	1							
material	condition	TYS (MPa)	UTS (MPa)	elongation (%)	corrosion medium	$v_{\rm corr}^{a}  ({\rm mm/y})$	$CR^{b}$ (mm/y)	referenc
Mg-1Gd	as-cast				9 g/L NaCl		24.50	55
Mg-3Gd	as-cast				9 g/L NaCl		0.21	55
Mg-5Gd	as-cast				9 g/L NaCl		0.32	55
Mg-2Gd	as-cast	38.0	103.7	6.4	1% NaCl		12.90	18
Mg-5Gd	as-cast	54.8	128.5	6.6	1% NaCl		3.52	18
Mg-10Gd	as-cast	84.1	131.2	2.5	1% NaCl		1.10	18
Mg-15Gd	as-cast	127.6	175.2	1.0	1% NaCl		16.76	18
Mg-2Gd	as-aged	41.3	101.4	5.7				18
Mg-5Gd	as-aged	42.6	78.7	4.3				18
Mg-10Gd	as-aged	85.4	132.3	2.2				18
Mg-15Gd	as-aged	201.4	250.9	0.7				18
Mg-3Gd	as-extruded				SBF		1.87	33
Mg-1Zn	as-cast				9 g/L NaCl		1.27	56
Mg-3Zn	as-cast				9 g/L NaCl		2.51	56
Mg-0.5Zn	as-cast	38	95	4.2	SBF	2.34	1.04	57
Mg-1.0Zn	as-cast	42	99	6.1	SBF	3.95	1.14	57
Mg-1.5Zn	as-cast	51	109	5.9	SBF	8.30	1.36	57
Mg-2.0Zn	as-cast	65	121	5.3	SBF	9.37	1.32	57
Mg-1Zn	as-cast	60.6	187.7	13.8	Hank's	0.53	2.01	58
Mg-5Zn	as-cast	75.6	194.6	8.5	Hank's	0.26	1.26	58
Mg-7Zn	as-cast	67.3	135.5	6.0	Hank's	1.17	3.18	57
Mg-0.5Zn	as-extruded	62	145	17.2	SBF	0.44	0.49	57
Mg-1.0Zn	as-extruded	91	169	18.7	SBF	0.63	0.54	57
Mg-1.5Zn	as-extruded	101	190	17.2	SBF	0.61	0.58	57
Mg-2.0Zn	as-extruded	111	198	15.7	SBF	0.64	0.61	
Mg-6Zn	as-extruded	169.5	279.5	18.8	SBF	0.16	0.20	38
Mg-1Ca	as-extruded	~135	240	10.6	Hank's	2.1		59 60,
MAGNEZIX	powder metallurgy	>250	>275	10				12
HP-Mg	as-rolled	156.3	225.8	13.9	Hank's	0.19	0.13	present v
Mg-1.0Zn-2.0Gd	as-rolled	168.0	225.8	33.5	Hank's	0.39	0.31	present v
Mg-1.8Zn-0.2Gd	as-rolled	272.2	288.1	16.1	Hank's	0.12	0.16	present v
Mg-1.8Zn-0.8Gd	as-rolled	250.1	318.1	14.2	Hank's	0.32	0.19	present v

<sup>&</sup>lt;sup>a</sup>v<sub>corr</sub>: corrosion rate calculated from polarization plots by using Tafel region extrapolation. <sup>b</sup>CR: corrosion rate calculated from the weight loss.

mechanical properties and corrosion resistance of our Mg-1.8Zn-0.2Gd and Mg-1.8Zn-0.8Gd alloys were mainly superior to those of other binary Mg-Zn and Mg-Gd alloys. In addition, the mechanical properties of the Mg-1.8Zn-0.2Gd alloy were comparable to those of MgYREZr alloy (matrix of MAGNEZIX screw), and the corrosion rate of this alloy was at a relatively low level (<0.28 mm/y in Hank's solution), as shown in Table 3. In vitro biocompatibility and in vivo tissue response of Mg-1.8Zn-0.2Gd has been wellguaranteed in our study. Total alloying additions in Mg-1.8Zn-0.2Gd were 2.0 wt %, and RE addition was minimized to as low as 0.2 wt %, significantly lower than that of WE43 (4 wt % Y + 3 wt % mischmetal). Possible biosafety problems with high RE-dosed alloys and uncertainties in mischmetal (complex RE compositions) strengthened alloys could be basically avoided. It can be concluded that mechanical strength, degradation behavior, and in vitro and in vivo biocompatibility of our Mg-1.8Zn-0.2Gd alloy could basically fulfill the requirements for nonload-bearing orthopedic implants.

**4.2. Concerns and Cautions.** Severely localized corrosion is detrimental to implant mechanical efficiency. Localized corrosion that happens in vivo should call for prompt attention. The nonuniform corrosion in vivo should be ascribed to impurities (Fe, Ni, Cu, and Co derived from raw materials or

introduced from the production processes) or inhomogeneous composition at local regions <sup>44</sup> and also might be caused by the implant surface defects. In addition, residual second phases or nonuniform distribution of second-phase particles could also lead to localized corrosion. Thus, uniform corrosion in vivo could be achieved by purification (reduce/eliminate adverse effects of impurities on corrosion), proper heat treatment, and plastic working process (microstructure control), to obtain well-controlled implant surface quality in the future.

The biocompatibility of Mg–Zn–Gd alloys mainly depends on the ion release and pH increase during implant degradation. The pH value surrounding the implant can be balanced by the host itself and adjusted by degradation control. Then, the dosage of the released metallic ions dominate the possible toxicity. Because the biocompatibility of Mg and Zn has been verified in many publications, possible toxicity of Mg–Zn–Gd alloys mainly depends on excessive Gd release. Accumulation of Gd in rat organs and disturbed bone remodeling were reported in a latest research, in which a magnesium alloy with a high Gd content (Mg–10Gd) was used.<sup>35</sup> Seriously, Gd addition in magnesium-based implants in the premise of enhancing mechanical properties and corrosion resistance should be controlled to as little as possible.

#### 5. CONCLUSIONS

Motivated by the attractive mechanical properties and corrosion resistance of Mg-Gd-based alloys, three magnesium alloys with a low combined-addition of Gd and Zn were developed. Mg-1.8Zn-0.2Gd was composed of a single  $\alpha$ -Mg phase. Besides α-Mg phase, Mg<sub>5</sub>Gd and Mg<sub>3</sub>Gd<sub>2</sub>Zn<sub>3</sub> were also detected in Mg-1.0Zn-2.0Gd and Mg-1.8Zn-0.8Gd. The mechanical properties of our Mg-1.8Zn-0.2Gd alloy were comparable to those of MgYREZr alloy (matrix of MAGNEZIX screw), with a decent corrosion rate. In addition, Mg-1.8Zn-0.2Gd exhibited no cytotoxicity to L929, MG63, and VSMC cells. Continuous degradation of the Mg-1.8Zn-0.2Gd implant in vivo could be found, and signs of localized corrosion could also be observed from the micro-CT analysis. The implant could maintain its structural integrity in the first 2 months, and only some residual parts could be detected after 6 months. All animals that received implantation survived, and no negative effects were observed histologically on bone tissues. The Mg-1.8Zn-0.2Gd implant showed fast osseointegration with the surrounding bones in the first 2 months and did not disturb bone remodeling. In summary, Mg-Zn-Gd alloys exhibit great potential for use as orthopedic implant materials on the condition that Gd content should be carefully controlled.

#### ASSOCIATED CONTENT

## **S** Supporting Information

The Supporting Information is available free of charge on the ACS Publications website at DOI: 10.1021/acsami.7b15498.

Ion release during in vitro corrosion, extract concentration (dilution) on cell viability and attachment, and typical LIVE/DEAD staining of various cells cultured in Mg-1.8Zn-0.2Gd extract for up to 5 days (PDF)

## AUTHOR INFORMATION

## **Corresponding Authors**

\*E-mail: yfzheng@pku.edu.cn. Phone/Fax: +86-10-62767411 (Y.Z.).

\*E-mail: jiangbaoguo@vip.sina.com (B.J.).

\*E-mail: rschen@imr.ac.cn (R.C.).

## ORCID

Yufeng Zheng: 0000-0002-7402-9979

#### **Author Contributions**

D.B. and J.D. designed and performed the experiments with assistance from N.L., X.C., Y.Z., Y.L., W.L., H.C., P.X., Z.G., and Y.K.; R.C. provided the experimental alloys; Y.Z. and B.J. supervised the project; D.B. prepared the manuscript; W.L., Y.Z., B.J., and R.C. contributed in language improvements and proof reading. All authors have given approval to the final version of the manuscript.

## Notes

The authors declare no competing financial interest.

# ■ ACKNOWLEDGMENTS

This work was supported by the National Key Research and Development Program of China (grant no. 2016YFC1102402), the National Natural Science Foundation of China (grant no. 51431002), the NSFC/RGC Joint Research Scheme (grant nos. 51361165101 and 5161101031), and the NSFC-RFBR Cooperation Project (grant no. 51611130054).

#### REFERENCES

- (1) Staiger, M. P.; Pietak, A. M.; Huadmai, J.; Dias, G. Magnesium and Its Alloys as Orthopedic Biomaterials: A Review. *Biomaterials* **2006**, *27*, 1728–1734.
- (2) Zheng, Y. F.; Gu, X. N.; Witte, F. Biodegradable Metals. *Mater. Sci. Eng.*, R **2014**, 77, 1–34.
- (3) Witte, F. Reprint of: The History of Biodegradable Magnesium Implants: A Review. *Acta Biomater.* **2015**, 23, S28–S40.
- (4) Zhao, D.; Witte, F.; Lu, F.; Wang, J.; Li, J.; Qin, L. Current Status on Clinical Applications of Magnesium-Based Orthopaedic Implants: A Review from Clinical Translational Perspective. *Biomaterials* **2017**, 112, 287–302.
- (5) Nagels, J.; Stokdijk, M.; Rozing, P. M. Stress Shielding and Bone Resorption in Shoulder Arthroplasty. *J. Shoulder Elbow Surg.* **2003**, *12*, 35–39.
- (6) Neacsu, P.; Ion, R. N.; Mitran, V.; Staras, A. I.; Cimpean, A. State of the Art and Recent Patents on Mg-Based Biodegradable Bone Implants. *Recent Pat. Regener. Med.* **2014**, *4*, 168–188.
- (7) Wong, H. M.; Zhao, Y.; Tam, V.; Wu, S.; Chu, P. K.; Zheng, Y.; To, M. K. T.; Leung, F. K. L.; Luk, K. D. K.; Cheung, K. M. C.; Yeung, K. W. K. In Vivo Stimulation of Bone Formation by Aluminum and Oxygen Plasma Surface-Modified Magnesium Implants. *Biomaterials* 2013, 34, 9863–9876.
- (8) Zhang, Y.; Xu, J.; Ruan, Y. C.; Yu, M. K.; O'Laughlin, M.; Wise, H.; Chen, D.; Tian, L.; Shi, D.; Wang, J.; Chen, S.; Feng, J. Q.; Chow, D. H. K.; Xie, X.; Zheng, L.; Huang, L.; Huang, S.; Leung, K.; Lu, N.; Zhao, L.; Li, H.; Zhao, D.; Guo, X.; Chan, K.; Witte, F.; Chan, H. C.; Zheng, Y.; Qin, L. Implant-Derived Magnesium Induces Local Neuronal Production of CGRP to Improve Bone-Fracture Healing in Rats. *Nat. Med.* **2016**, 22, 1160–1169.
- (9) Saris, N.-E. L.; Mervaala, E.; Karppanen, H.; Khawaja, J. A.; Lewenstam, A. Magnesium: An Update on Physiological, Clinical and Analytical Aspects. *Clin. Chim. Acta* **2000**, *294*, 1–26.
- (10) Watson, R. R.; Preedy, V. R.; Zibadi, S. Magnesium in Human Health and Disease; Humana Press, 2013.
- (11) Windhagen, H.; Radtke, K.; Weizbauer, A.; Diekmann, J.; Noll, Y.; Kreimeyer, U.; Schavan, R.; Stukenborg-Colsman, C.; Waizy, H. Biodegradable Magnesium-Based Screw Clinically Equivalent to Titanium Screw in Hallux Valgus Surgery: Short Term Results of the First Prospective, Randomized, Controlled Clinical Pilot Study. *Biomed. Eng. Online* **2013**, *12*, 62.
- (12) Waizy, H.; Diekmann, J.; Weizbauer, A.; Reifenrath, J.; Bartsch, I.; Neubert, V.; Schavan, R.; Windhagen, H. In Vivo Study of a Biodegradable Orthopedic Screw (MgYREZr-Alloy) in a Rabbit Model for up to 12 Months. *J. Biomater. Appl.* **2014**, 28, 667–675.
- (13) Haude, M.; Ince, H.; Abizaid, A.; Toelg, R.; Lemos, P. A.; von Birgelen, C.; Christiansen, E. H.; Wijns, W.; Neumann, F.-J.; Kaiser, C.; Eeckhout, E.; Lim, S. T.; Escaned, J.; Garcia-Garcia, H. M.; Waksman, R. Safety and Performance of the Second-Generation Drug-Eluting Absorbable Metal Scaffold in Patients with De-Novo Coronary Artery Lesions (BIOSOLVE-II): 6 Month Results of a Prospective, Multicentre, Non-Randomised, First-in-Man Trial. *Lancet* 2016, 387, 31–39.
- (14) http://www.magmaris.com/en/newsroom/june-15-2016 (last accessed on October 6, 2017).
- (15) Han, P.; Cheng, P.; Zhang, S.; Zhao, C.; Ni, J.; Zhang, Y.; Zhong, W.; Hou, P.; Zhang, X.; Zheng, Y.; Chai, Y. In Vitro and in Vivo Studies on the Degradation of High-Purity Mg (99.99wt.%) Screw with Femoral Intracondylar Fractured Rabbit Model. *Biomaterials* 2015, 64, 57–69.
- (16) Gu, X. N.; Zhou, W. R.; Zheng, Y. F.; Cheng, Y.; Wei, S. C.; Zhong, S. P.; Xi, T. F.; Chen, L. J. Corrosion Fatigue Behaviors of Two Biomedical Mg Alloys—AZ91D and WE43—In Simulated Body Fluid. *Acta Biomater.* **2010**, *6*, 4605–4613.
- (17) Elektron 43 Extruded Products. https://www.magnesium-elektron.com/wp-content/uploads/2016/10/Elektron-43-Extruded-Products\_0.pdf (last accessed on October 6, 2017).
- (18) Hort, N.; Huang, Y.; Fechner, D.; Störmer, M.; Blawert, C.; Witte, F.; Vogt, C.; Drücker, H.; Willumeit, R.; Kainer, K. U.

- Magnesium Alloys as Implant Materials—Principles of Property Design for Mg—RE Alloys. *Acta Biomater.* **2010**, *6*, 1714—1725.
- (19) Wu, D.; Chen, R. S.; Han, E. H. Excellent Room-Temperature Ductility and Formability of Rolled Mg-Gd-Zn Alloy Sheets. *J. Alloys Compd.* **2011**, 509, 2856–2863.
- (20) Zhen, R.; Sun, Y.; Xue, F.; Sun, J.; Bai, J. Effect of Heat Treatment on the Microstructures and Mechanical Properties of the Extruded Mg-11Gd-1Zn Alloy. *J. Alloys Compd.* **2013**, 550, 273–278
- (21) Yamasaki, M.; Anan, T.; Yoshimoto, S.; Kawamura, Y. Mechanical Properties of Warm-Extruded Mg–Zn–Gd Alloy with Coherent 14H Long Periodic Stacking Ordered Structure Precipitate. *Scr. Mater.* **2005**, *53*, 799–803.
- (22) Li, R. G.; Nie, J. F.; Huang, G. J.; Xin, Y. C.; Liu, Q. Development of High-Strength Magnesium Alloys via Combined Processes of Extrusion, Rolling and Ageing. *Scr. Mater.* **2011**, *64*, 950–953.
- (23) Liu, K.; Wang, X.; Du, W. Development of Extraordinary High-Strength-Toughness Mg Alloy via Combined Processes of Repeated Plastic Working and Hot Extrusion. *Mater. Sci. Eng., A* **2013**, *573*, 127–131.
- (24) Xu, C.; Zheng, M. Y.; Xu, S. W.; Wu, K.; Wang, E. D.; Kamado, S.; Wang, G. J.; Lv, X. Y. Ultra High-Strength Mg—Gd—Y—Zn—Zr Alloy Sheets Processed by Large-Strain Hot Rolling and Ageing. *Mater. Sci. Eng., A* **2012**, *547*, 93—98.
- (25) Nayeb-Hashemi, A. A. Phase Diagrams of Binary Magnesium Alloys; ASM International: Metals Park, OH, 1998.
- (26) Liu, W.; Cao, F.; Chang, L.; Zhang, Z.; Zhang, J. Effect of Rare Earth Element Ce and La on Corrosion Behavior of AM60 Magnesium Alloy. *Corros. Sci.* **2009**, *51*, 1334–1343.
- (27) Haley, T. J. Pharmacology and Toxicology of the Rare Earth Elements. J. Pharm. Sci. 1965, 54, 663-670.
- (28) Haley, T. J.; Raymond, K.; Komesu, N.; Upham, H. C. Toxicological and Pharmacological Effects of Gadolinium and Samarium Chlorides. *Br. J. Pharmacol. Chemother.* **1961**, 17, 526–532.
- (29) De Roos, A.; Doornbos, J.; Baleriaux, D.; Bloem, H. L.; Falke, T. H. Clinical Applications of Gadolinium-DTPA in MRI. *Magn. Reson. Annu.* **1988**, 113–145.
- (30) Ratzinger, G.; Agrawal, P.; Körner, W.; Lonkai, J.; Sanders, H. M. H. F.; Terreno, E.; Wirth, M.; Strijkers, G. J.; Nicolay, K.; Gabor, F. Surface Modification of PLGA Nanospheres with Gd-DTPA and Gd-DOTA for High-Relaxivity MRI Contrast Agents. *Biomaterials* **2010**, *31*, 8716–8723.
- (31) Bruce, D. W.; Hietbrink, B. E.; DuBois, K. P. The Acute Mammalian Toxicity of Rare Earth Nitrates and Oxides. *Toxicol. Appl. Pharmacol.* **1963**, *5*, 750–759.
- (32) Feyerabend, F.; Fischer, J.; Holtz, J.; Witte, F.; Willumeit, R.; Drücker, H.; Vogt, C.; Hort, N. Evaluation of Short-Term Effects of Rare Earth and Other Elements Used in Magnesium Alloys on Primary Cells and Cell Lines. *Acta Biomater.* **2010**, *6*, 1834–1842.
- (33) Guo, Y.; Liu, W.; Ma, S.; Wang, J.; Zou, J.; Liu, Z.; Zhao, J.; Zhou, Y. A Preliminary Study for Novel Use of Two Mg Alloys (WE43 and Mg3Gd). *J. Mater. Sci.: Mater. Med.* **2016**, *27*, 82.
- (34) Myrissa, A.; Agha, N. A.; Lu, Y.; Martinelli, E.; Eichler, J.; Szakács, G.; Kleinhans, C.; Willumeit-Römer, R.; Schäfer, U.; Weinberg, A.-M. In Vitro and in Vivo Comparison of Binary Mg Alloys and Pure Mg. *Mater. Sci. Eng., C* **2016**, *61*, 865–874.
- (35) Myrissa, A.; Braeuer, S.; Martinelli, E.; Willumeit-Römer, R.; Goessler, W.; Weinberg, A. M. Gadolinium Accumulation in Organs of Sprague—Dawley Rats after Implantation of a Biodegradable Magnesium-Gadolinium Alloy. *Acta Biomater.* **2017**, *48*, 521–529.
- (36) Chen, Y.; Xu, Z.; Smith, C.; Sankar, J. Recent Advances on the Development of Magnesium Alloys for Biodegradable Implants. *Acta Biomater.* **2014**, *10*, 4561–4573.
- (37) Hradilová, M.; Vojtěch, D.; Kubásek, J.; Čapek, J.; Vlach, M. Structural and Mechanical Characteristics of Mg–4Zn and Mg–4Zn–0.4Ca Alloys after Different Thermal and Mechanical Processing Routes. *Mater. Sci. Eng., A* 2013, 586, 284–291.

- (38) Zhang, S.; Zhang, X.; Zhao, C.; Li, J.; Song, Y.; Xie, C.; Tao, H.; Zhang, Y.; He, Y.; Jiang, Y. Research on an Mg–Zn Alloy as a Degradable Biomaterial. *Acta Biomater.* **2010**, *6*, 626–640.
- (39) Li, H.; He, W.; Pang, S.; Liaw, P. K.; Zhang, T. In Vitro Responses of Bone-Forming MC3T3-E1 Pre-Osteoblasts to Biodegradable Mg-Based Bulk Metallic Glasses. *Mater. Sci. Eng., C* **2016**, *68*, 632–641.
- (40) Yan, H.; Chen, R. S.; Han, E. H. Room-Temperature Ductility and Anisotropy of Two Rolled Mg–Zn–Gd Alloys. *Mater. Sci. Eng., A* **2010**, 527, 3317–3322.
- (41) ASTM-E8-04. Standard Test Methods for Tension Testing of Metallic Materials. *Annual Book of ASTM Standards*; American Society for Testing and Materials: Philadelphia, PA, 2004.
- (42) Ng, W. F.; Chiu, K. Y.; Cheng, F. T. Effect of pH on the in Vitro Corrosion Rate of Magnesium Degradable Implant Material. *Mater. Sci. Eng.*, C 2010, 30, 898–903.
- (43) ASTM G31-72. Standard Practice for Laboratory Immersion Corrosion Testing of Metals. J. ASTM Int., 2004.
- (44) Song, G.; Atrens, A. Understanding Magnesium Corrosion—A Framework for Improved Alloy Performance. *Adv. Eng. Mater.* **2003**, *5*, 837–858.
- (45) ASTM-G1-90. Standard Practice for Preparing, Cleaning, and Evaluating Corrosion Test Specimens. *Annual Book of ASTM Standards*; American Society for Testing and Materials: West Conshohocken, PA, 1999.
- (46) Shi, Z.; Liu, M.; Atrens, A. Measurement of the Corrosion Rate of Magnesium Alloys Using Tafel Extrapolation. *Corros. Sci.* **2010**, *52*, 579–588.
- (47) ISO 10993-5:2009(E). Biological Evaluation of Medical Devices—Part 5: Tests for in Vitro Cytotoxicity; International Organization for Standardization, 2009.
- (48) Xiu, P.; Jia, Z.; Lv, J.; Yin, C.; Cheng, Y.; Zhang, K.; Song, C.; Leng, H.; Zheng, Y.; Cai, H. Tailored Surface Treatment of 3D Printed Porous Ti6Al4V by Micro-Arc Oxidation for Enhanced Osseointegration via Optimized Bone In-Growth Patterns and Interlocked Bone/Implant Interface. ACS Appl. Mater. Interfaces 2016, 8, 17964–17975.
- (49) Li, Z.; Song, G.-L.; Song, S. Effect of Bicarbonate on Biodegradation Behaviour of Pure Magnesium in a Simulated Body Fluid. *Electrochim. Electrochim. Acta* **2014**, *115*, 56–65.
- (50) Mueller, W.-D.; de Mele, M. F. L.; Nascimento, M. L.; Zeddies, M. Degradation of Magnesium and Its Alloys: Dependence on the Composition of the Synthetic Biological Media. *J. Biomed. Mater. Res., Part A* **2009**, 90, 487–495.
- (51) Song, G. Control of Biodegradation of Biocompatable Magnesium Alloys. *Corros. Sci.* **2007**, *49*, 1696–1701.
- (52) Sanchez, A. H. M.; Luthringer, B. J. C.; Feyerabend, F.; Willumeit, R. Mg and Mg Alloys: How Comparable Are in Vitro and in Vivo Corrosion Rates? A Review. *Acta Biomater.* **2015**, *13*, 16–31.
- (53) Yamamoto, A.; Hiromoto, S. Effect of Inorganic Salts, Amino Acids and Proteins on the Degradation of Pure Magnesium in Vitro. *Mater. Sci. Eng., C* **2009**, *29*, 1559–1568.
- (54) Willumeit, R.; Fischer, J.; Feyerabend, F.; Hort, N.; Bismayer, U.; Heidrich, S.; Mihailova, B. Chemical Surface Alteration of Biodegradable Magnesium Exposed to Corrosion Media. *Acta Biomater.* **2011**, *7*, 2704–2715.
- (55) Kubásek, J.; Vojtěch, D. Structural and Corrosion Characterization of Biodegradable Mg–RE (RE=Gd, Y, Nd) Alloys. *Trans. Nonferrous Met. Soc. China* **2013**, 23, 1215–1225.
- (56) Kubásek, J.; Vojtěch, D. Structural Characteristics and Corrosion Behavior of Biodegradable Mg–Zn, Mg–Zn–Gd Alloys. *J. Mater. Sci.: Mater. Med.* **2013**, 24, 1615–1626.
- (57) Peng, Q.; Li, X.; Ma, N.; Liu, R.; Zhang, H. Effects of Backward Extrusion on Mechanical and Degradation Properties of Mg–Zn Biomaterial. *J. Mech. Behav. Biomed. Mater.* **2012**, *10*, 128–137.
- (58) Cai, S.; Lei, T.; Li, N.; Feng, F. Effects of Zn on Microstructure, Mechanical Properties and Corrosion Behavior of Mg–Zn Alloys. *Mater. Sci. Eng., C* **2012**, 32, 2570–2577.
- (59) Liu, Y.; Bian, D.; Wu, Y.; Li, N.; Qiu, K.; Zheng, Y.; Han, Y. Influence of Biocompatible Metal Ions (Ag, Fe, Y) on the Surface

Chemistry, Corrosion Behavior and Cytocompatibility of Mg-1Ca Alloy Treated with MEVVA. *Colloids Surf., B* **2015**, *133*, 99–107. (60) Li, Z.; Gu, X.; Lou, S.; Zheng, Y. The Development of Binary Mg-Ca Alloys for Use as Biodegradable Materials within Bone. *Biomaterials* **2008**, *29*, 1329–1344.